Iterative static ΔB0 field map estimation for off-resonance correction in non-Cartesian susceptibility weighted imaging

Guillaume Daval-Frérot, Aurélien Massire, Boris Mailhé, Mariappan S. Nadar, Alexandre Vignaud, Philippe Ciuciu

FULL PAPER

Iterative static ΔB_0 field map estimation for off-resonance correction in non-Cartesian susceptibility weighted imaging

Guillaume Daval-Frérot[1,2,3] | Aurélien Massire[1] | Boris Mailhe[4] | Mariappan Nadar[4] | Alexandre Vignaud[2] | Philippe Ciuciu[2,3]

[1]Siemens Healthcare SAS, Saint-Denis, 93210, France

[2]CEA, NeuroSpin, CNRS, Université Paris-Saclay, Gif-sur-Yvette, 91191, France

[3]Inria, Parietal, Palaiseau, 91120, France

[4]Siemens Healthineers, Digital Technology & Innovation, Princeton, 08540, NJ, USA

Correspondence
Philippe Ciuciu PhD, NeuroSpin, CEA, Gif-sur-Yvette, 91191, France
Email: philippe.ciuciu@cea.fr

Purpose: Patient-induced inhomogeneities in the magnetic field cause distortions and blurring during acquisitions with long readouts such as in susceptibility-weighted imaging (SWI). Most correction methods require collecting an additional ΔB_0 field map to remove these artifacts.

Theory: The static ΔB_0 field map can be approximated with an acceptable error directly from a single echo acquisition in SWI. The main component of the observed phase is linearly related to ΔB_0 and the echo time TE, and the relative impact of non-ΔB_0 terms becomes insignificant with TE>20ms at 3T for a well-tuned system.

Methods: The main step is to combine and unfold the multi-channel phase maps wrapped many times, and several competing algorithms are compared for this purpose. Four in vivo brain data sets collected using the recently proposed 3D SPARKLING readouts are used to assess the proposed method.

Results: The estimated 3D field maps generated with a 0.6 mm isotropic spatial resolution provide overall similar off-resonance corrections compared to reference corrections based on an external ΔB_0 acquisitions, and even improved for two out of four individuals. Although a small estimation error is expected, no aftermath was observed in the proposed corrections, while degradations were observed in the references.

Conclusion: A static ΔB_0 field map estimation method was proposed to take advantage of acquisitions with long echo times, and outperformed the reference technique based on an external field map. The difference can be attributed to an inherent robustness to mismatches between volumes and external ΔB_0 maps, and diverse other sources investigated.

KEYWORDS
SWI, ΔB_0 field map estimation, non-Cartesian imaging, compressed sensing, SPARKLING

1 | INTRODUCTION

Susceptibility-weighted imaging (SWI) [1] is commonly used in high resolution brain venography or traumatic brain injuries for its sensitivity to blood products and calcium [2]. The magnetic susceptibility of those compounds contributes to local field distortions visible on filtered phase maps. Long echo times (e.g. TE $\simeq 20-40$ms at 3T) are typically used to enhance the susceptibility contribution, resulting in compromises on slice thickness to reach clinically acceptable scan times. Many parallel imaging and compressed-sensing (CS) methods [3, 4, 5, 6, 7, 8, 9] have been proposed over the last two decades to accelerate MRI acquisitions and non-Cartesian sampling patterns [10, 11] have recently gained popularity. In particular, the trajectories based on the Spreading Projection Algorithm for Rapid K-space sampLING (SPARKLING) in 2D [11] and 3D imaging [12, 13] can reach acceleration factor (AF) superior to 15 in scan times compared to fully sampled Cartesian imaging in high resolution (0.6 mm) isotropic brain imaging by taking advantage of all degrees of freedom offered by modern MR scanners and long observation windows (i.e. readouts) [13]. However this experimental setting also results in off-resonance artifacts amplification that causes geometric distortions and image blurring [14]. These artifacts are mainly caused by patient-induced static B_0 field inhomogeneities which are especially pronounced near air-tissue interfaces, for instance close to the oral cavity and the ear canals. Non-Cartesian sampling patterns tend to be more sensitive to B_0 inhomogeneities causing local k-space inconsistencies over the different gradient directions [15]. Therefore, specific attention must be paid to reduce signal and detail dropouts in these regions.

Different approaches exist to compensate for off-resonance artifacts during the acquisitions or later on in image reconstruction or post-processing. The default technique integrated in all scanners is the spherical harmonic shimming [14, 16] that allows the partial mitigation of patient-induced static inhomogeneities using a set of shim coils. A ΔB_0 field map is acquired and minimized with respect to the gradients which are expanded over a spherical harmonic basis (generally up to the second or third order). This calibration step is performed quickly using a low resolution map since the technique does not allow precise correction [17]. Although this approach provides a significant improvement on image quality, a complementary technique is required in the most demanding setups such as in EPI [18, 19] or in non-Cartesian imaging that makes use of long readouts [20, 21, 22, 12, 13]. Recent works have been proposed to improve this method using more efficient coil designs [23] that accurately fit the expected inhomogeneity profiles [24] using complementary data. Those experimental results permit to achieve improved correction performances but remain however limited by the number of shimming coils to be deployed in order to reach the theoretical limits [25]. For that reason, alternative retrospective approaches are instrumental in correcting off-resonance effects once the k-space data has been collected.

In the particular case of Cartesian EPI, a well-known technique [26, 27] consists in inverting the gradient direction at every time frame to emphasize the geometric distortions and thus obtain a deformation map which can then be directly corrected. This technique is however difficult to transpose to non-Cartesian readouts (e.g. spirals [20, 21, 22], rosette [28], SPARKLING [11, 12, 13]) as the gradient directions are strongly varying along multiple dimensions simultaneously. In such context, a more generic and well-established method [29, 30, 31, 32, 33] consists in compensating the undesired ΔB_0 gradient by modifying the Fourier operator to integrate the prior knowledge of a ΔB_0 field map. This technique can be applied to both Cartesian and non-Cartesian data at the cost of much longer (e.g. 15-fold) image reconstruction times.

For multi-echo sequences, the ΔB_0 field map can be directly derived from the acquisitions [14]. For single echo sequences, the constraint of knowing the ΔB_0 field map has been considered from different perspectives in the literature [34, 35, 36, 37, 38, 39] to avoid additional medium-to-high resolution multi-echo acquisitions that would counterbalance the goal of accelerating the original scan. A first solution is to integrate

the multiple echoes into the desired sequences [40, 41], however they represent an additional constraint on the pulse sequence design that is not compatible with some protocols due to their long readouts. This holds in particular for multishot spiral [22], segmented EPI [18] or SPARKLING [13] imaging. Post-processing approaches have thus been developed, notably by the teams that contributed to the correction method [34, 35]. One of the most popular approaches over the years initiated by Sutton et al. [35] is to solve a non-convex optimization problem involving the ΔB_0 extended signal equation model during image reconstruction. Recent developments [36, 37] rely on tight regularizing constraints to make the solution locally smooth by projecting the gradients onto a set of functions (e.g. 2D Gaussians). Compared to the original implementation [35], this approach guarantees a successful convergence to a local minimizer. However, the field maps shown in [37] are low resolution due to the involved smoothing constraints. Another possibility lies in the simulation of the ΔB_0 field map [38, 39] with mask-sensitive binary anatomy models, however proposing an accurate mask is challenging without even considering the model limitations. As the stated non-Cartesian SWI problem arises from long readouts centered over long echo times, in this paper we propose to take advantage of the phase properties in such context. Indeed the ΔB_0 contribution to the phase maps grows linearly with TE [42] and becomes significantly dominating while most other contributions remain constant or decay [14, 43, 44]. The disproportion reaches a point where it can be assumed that the phase is equivalent to the ΔB_0 field map with minimal error.

In this work, a pipeline is proposed to convert the phase map extracted either from a spherical stack of 2D SPARKLING trajectories [12] or from full 3D SPARKLING ones [13] into a high resolution 3D ΔB_0 field map that is subsequently used to correct the SWI acquisition for B_0 inhomogeneities. These SPARKLING trajectories were specifically designed for SWI acquisitions with different acceleration factors (as defined later in Eq. (10)). The iterative procedure requires notably to address the problems of coil combination [45, 46, 47, 48, 49] and phase unwrapping [50, 51, 52, 53] for which two and four algorithms respectively were jointly confronted. On four healthy volunteers at 3 Tesla, the ΔB_0 field map estimates in the brain are directly compared to the individually-matched acquired references and the benefit of this internal estimation is subsequently assessed on SWI brain images after offline image reconstruction.

2 | THEORY

The simplest model [54] to recover a complex-valued MR image f from an acquired complex-valued signal s over time window T_{obs} at the grid position r from k-space trajectory k is:

$$f(r) = \int_{T_{obs}} s(t) e^{i2\pi k(t)\cdot r} dt \tag{1}$$

The above equation corresponds to an adjoint Fourier transform of the raw data. However, this model does not account for the different perturbations of the signal s that occur during acquisition. A common extension that allows the recovery of a partially corrected image $\widehat{f}$ for the undesired effects of B_0 field inhomogeneities reads as follows:

$$\widehat{f}(r) = \int_{T_{obs}} s(t) e^{i2\pi(k(t)\cdot r + \Delta B_0(r)t)} dt \tag{2}$$

The additional gradient term within the exponential assumes the knowledge of the ΔB_0 field map. The most common method [14] to find it relies on the measurements of phase maps. Indeed, the observed phase ϕ_{obs} of an MR image f at position r can be linked to the ΔB_0 field map as follows:

$$\phi_{obs}(r) \equiv \phi(r) \ (\text{mod } 2\pi) \tag{3}$$

$$\phi(r) = \phi_{\Delta B_0}(r) + \phi_{\Delta B_1^{\pm}}(r) + \phi_{B_e}(r) + \phi_{others}(r) \tag{4}$$

where $\phi_{\Delta B_0}$, $\phi_{\Delta B_1^{\pm}}$, and ϕ_{B_e} are the phase contributions emanating from major sources: inhomogeneities in the

B_0 and B_1 fields for the first two terms, and B_e field induced by eddy currents for the third one. The ϕ_{others} term includes the effect of minor sources such as heating and physiological motion. A common approximation is to consider ΔB_0 related to the echo time TE through a linear relationship [14, 42]:

$$\phi_{\Delta B_0}(r, TE) = 2\pi\, TE\, \Delta B_0(r) \tag{5}$$

The common approach to estimate a ΔB_0 map is to perform acquisitions with multiple echo times [14], and consider other phase contributions as constant with respect to TE. For example, considering two echo times such that $TE_1 < TE_2$, we obtain:

$$\Delta B_0(r) = \frac{\phi(r, TE_2) - \phi(r, TE_1)}{2\pi(TE_2 - TE_1)} \tag{6}$$

This formulation implies that ϕ must be recovered from ϕ_{obs} by solving Eq. (3). Although many unwrapping algorithms have been proposed in the literature [55, 50, 51, 52, 53], convenient analytical choices are preferred to reduce the observed wrapping, and thus simplify or even avoid this step, such as applying a division over the complex-valued volumes acquired with close echo times [14]. In contrast, our approach consists in taking advantage of acquisitions with long echo times to propose a high resolution ΔB_0 map based on the phase image from a single echo SWI acquisition through the following approximation:

$$\Delta B_0(r) = \frac{\phi(r)}{2\pi\, TE} \tag{7}$$

considering that other contributions are almost negligible for long echo times at high magnetic field for well-tuned MR scanners [45, 56, 57, 58, 59]. Indeed the absolute error ϵ in the previous approximation can be decomposed into individually measurable contributions:

$$\epsilon(r) = \left| \frac{\phi_{\Delta B_1^{\pm}}(r) + \phi_{B_e}(r) + \phi_{others}(r)}{2\pi TE} \right| \tag{8}$$

The main component in Eq. (8) is $\phi_{\Delta B_1^{\pm}}$ as it includes both the radiofrequency pulse inhomogeneities and the coil sensitivities. An optimal coil combination with respect to the signal-to-noise ratio (SNR) can be computed when the coil sensitivity maps are known [45]. Similarly to the ΔB_0 map, these sensitivity maps require an additional acquisition and are therefore usually unknown. Various methods exist to estimate them from the acquired multi-channel volume [45, 46, 47]. After recombination, a constant phase shift ϕ_0 remains undetermined depending on the reference coil [60]. This term can be simply removed if we assume that a zero-order B_0 shimming is applied and matches the acquisition box as no constant term is expected any longer. Both coil combination algorithms and zero-order B_0 shimming hypothesis are considered in later experiments.

The additional fields created by the radiofrequency pulse inhomogeneities and the eddy currents [14, 43, 44] through the MR scanner and the coil are generally limited for well-designed and calibrated hardware [56, 57]. An experiment on oil phantom proposed in the supplementary materials (Section S1) suggests an error inferior to 2 Hz from the eddy currents contribution in the proposed experimental setup. However, the relative contribution of both sources increases with the B_0 field strength and may have a significant impact on the ΔB_0 estimation at very high magnetic fields [61, 62]. Overall, the related error at 3 Tesla is expected to be inferior to 10 Hz [45, 56, 57] on average while off-resonance frequencies can reach up to 300 Hz.

Based on the literature, other sources such as heating [58] and physiological motion [59] can be neglected for static contributions. Note that the contribution from heating follows a similar relationship with respect to TE [58] but is still considered negligible:

$$\phi_{\Delta T}(r, TE) = 2\pi\, TE\, \nu\, \alpha\, \Delta T(r) \tag{9}$$

where ν is the Larmor frequency and α the frequency shift per degree Celsius while ΔT refers to the temperature variation at voxel r.

Stronger motion such as bulk motion during the sequence acquisition could greatly impede the estimation. This issue is considered to be addressed sepa-

rately, as it would also hinder the overall quality of the images. Different methods exist to correct motion artifacts [63, 64], however the current clinical practice is to simply repeat the exam. Note that avoiding the ΔB_0 map acquisition already allows us to ignore potential inter-acquisitions mismatches caused by such motions. Overall, the main contributions to the estimation error ϵ are the radiofrequency pulse inhomogeneities, coils sensitivity and eddy currents [56, 57], along with an undetermined constant phase term supposedly close to zero.

Finally, the contribution from magnetic susceptibility of tissues has to be specifically preserved in the case of SWI. Indeed the susceptibility information, used to enhance diverse contrast sensitivities [2], originates from minor B_0 inhomogeneities [1, 14] and thus the estimated ΔB_0 field map should exclude those contributions to avoid cancelling them during the off-resonance correction. Since that information is usually extracted from high frequencies using filters [1], similar filters can be used over the ΔB_0 field map to remove this information from the correction step.

3 | METHODS

Our contribution is threefold: first, different algorithms for coil combination and phase unwrapping are jointly studied. Second, the best combination is integrated into an iterative pipeline aiming to estimate the ΔB_0 field map. Third, this map is used to perform off-resonance correction on the acquired k-space data. The performance of the later is evaluated by comparisons with corrections obtained from external ΔB_0 field maps.

3.1 | Coil combination and phase unwrapping

A particular attention has been paid to the above mentioned critical steps, namely the coil combination and phase unwrapping. Multiple algorithms have been jointly evaluated in order to reach an accurate and reliable estimation.

In regards to the coil combination, the technique developed by Parker et al. [46] referred here to as virtual coil combination (VCC) appears as the state of the art among the phase-preserving techniques [60]. Another method introduced by Walsh et al. [47], referred here to as adaptive coil combination (ACC), has been improved contemporarily by Inati et al. [48] to specifically preserve phase during combination. Both algorithms were internally implemented on graphical processing units (GPU) in Python [65] using the `CuPy`[1] module [66], with specific modifications to the ACC method detailed in the supplementary materials (Section S2).

For phase unwrapping, a total of four algorithms [50, 51, 53, 52] were considered to compare different approaches [67]. Only the method from Ghiglia et al. [50] was implemented internally on GPU, with noticeable changes described in the supplementary materials (Section S3) to extend it to 3D imaging. The other approaches were tested on CPU thanks to different open-source implementations: `scikit-image`[2] [68] in Python for Herráez et al. [51], the original implementation of ROMEO[3] in Julia [69] by Dymerska et al. [53] and `PyMRT`[4] [70] in Python for Schofield et al. [52]. The method from Ghiglia et al. [50] was the only one observed to benefit from masking the phase before application, so the others were not masked by default. Additionally, the method developed by Dymerska et al. [53] was used along with the magnitude information, as recommended by the authors.

A qualitative evaluation of the estimated maps by visual inspection after one iteration was performed over four volumes. The main criterion was to avoid anomalies in the ΔB_0 regions and outside the skull where the phase is locally inconsistent due to a void signal. The second criterion was to obtain off-resonance values as close as possible to the acquired ΔB_0 map used as reference.

[1] `https://github.com/cupy/cupy`
[2] `https://github.com/scikit-image/scikit-image`
[3] `https://github.com/korbinian90/ROMEO`
[4] `https://github.com/norok2/pymrt`

3.2 | ΔB_0 field map estimation

The ΔB_0 map estimation pipeline is represented in Fig. 1. First, the non-Cartesian multi-coil k-space data was compressed using the principal component analysis-based method proposed by Buehrer et al. [71]. The channel dimension is reduced to 30 components for image reconstruction, and to 5 components for the ΔB_0 map estimation. Then, an adjoint non-uniform fast Fourier transform (NUFFT) [72] with a pre-computed density compensation [73] was applied to the 5 compressed channels to produce multi-channel complex-valued volumes. The different channels were combined using the ACC method [47] and the resulting magnitude image was used to produce a brain mask, then combined with magnitude and phase images.

At this stage, the observed phase ϕ_{obs} remains wrapped over the (-π, π] domain. Phase unwrapping was performed using the algorithm proposed in [50] which consists in solving a Poisson equation weighted by the previously computed magnitude image. Finally, the phase maps were scaled by $1/2\pi\, TE$ following Eq. (7) and a low-pass filter was applied using a Hanning window over the central third of the Fourier domain. This filtering step is specific to SWI and is carried out to preserve the susceptibility contributions in the high frequencies during the ΔB_0 correction. This point is detailed in the supplementary materials (Section S6). Other contrasts relying on phase information might also require specific ΔB_0 map processing.

A first estimation of the ΔB_0 map is thus computed. For highly accelerated acquisitions (e.g. AF > 15 as defined below in Eq. (10)), the SNR in the ΔB_0 regions can be too low to provide an accurate field map. Therefore, the process should be iterated to improve the first estimation as shown in Fig. 1. In the next iterations, the regular NUFFT operator is replaced by a correcting pseudo-NUFFT operator [32], combined with the previous ΔB_0 estimation. This step actually consists of interpolating the usually intractable gradient compensation through a weighted sum of regular NUFFT operators. The histogram-based coefficients were used as weights with a number of interpolators $L = \lceil(\Delta B_{0_{max}} - \Delta B_{0_{min}})/25\rceil$ to maintain an approximation root mean square error (RMSE) below 10^{-5}. This way, some signal is recovered in regions where some of the inhomogeneities are being removed. The updated ΔB_0 map estimate provides information about previously missed inhomogeneities, and is thus added to the previous one(s) until convergence. Hence, the resulting map is also corrected for geometric distortions caused by B_0 inhomogeneities. In the following experiments, three additional iterations were run to reach convergence, based on experiments available in the supplementary materials (Section S5).

3.3 | Data acquisition and reconstruction

A total of four SWI volumes were acquired with non-Cartesian 3D GRE sequences, each on a different healthy volunteer at 3T (Magnetom Prisma^{FIT}, Siemens Healthcare, Erlangen, Germany) with a 64-channel head/neck coil array. The protocol has been approved by local and national ethical committees, and written consent was obtained from the volunteers. Two different sampling patterns were used with distinct acceleration factors defined as:

$$AF = \frac{N \times N_z}{N_c} \tag{10}$$

with N the in-plane resolution, N_z the number of slices and N_c the number of spokes. The recently proposed 3D spherical stack of SPARKLING [12] was used for two volumes (referred to as #1 and #2) with AF=10, and its recent extension, namely full 3D SPARKLING [13], was considered for the other two (referred to as #3 and #4) with AF=20. All acquisitions were performed with the following parameters: a 0.6 mm isotropic resolution, a field-of-view of 24 cm in-plane (N=384) over 12.5 cm (N_z=208), an observation time of T_{obs} = 20.48 ms centered around an echo time TE = 20 ms, a repetition time TR = 37 ms. For the spherical stack of SPARKLING acquisitions (#1, #2), we used a dwell time δt = 5 μs, and a number of spokes N_c=8192 that resulted in an acquisition time of 5 min. For the full 3D SPARKLING (#3,

#4), a smaller dwell time $\delta t = 2\ \mu$s was used to balance the smaller number of spokes N_c=4096 that resulted in a shorter acquisition of 2 min 30 s. For comparison purposes, an additional reference ΔB_0 map was acquired with a 2D GRE sequence using the following parameters: an acquisition time of 2 min 43 s (no acceleration), same field-of-view, a 2 mm isotropic resolution, two echo times $TE_1 = 4.92$ ms and $TE_2 = 7.38$ ms. Those echo times allow for an excursion of $\pm$ 203 Hz, resulting in one phase wrap present in all references and unwrapped using the method proposed by Herráez et al. [51].

MR image reconstruction was performed offline using the `pysap-mri`[5] software [74, 75] (cf. Fig. 1, C) which implements 3D self-calibrated compressed sensing reconstruction (ℓ_1-norm regularization in the wavelet domain using symlet 8 and 3 scales of decomposition) [76]. The ΔB_0 correction was performed using the approximation described in [32], with the number of interpolators L chosen as mentioned previously. Overall, the volumes were reconstructed considering three competing strategies: without correction, with correction based on the acquired ΔB_0 field map used as a reference, and with correction based on the estimated ΔB_0 field map. Further details about the offline reconstruction and correction are given in the supplementary materials (Section S4).

Finally, SWI specific processing as described in [1] was applied. The low frequencies were extracted by applying a Hanning window over the central third of the k-space, before being removed from the phase image to obtain a high frequency map, subsequently normalized to produce a continuous mask. The magnitude image was multiplied five times by the mask, and a minimum-intensity projection (mIP) was computed using a thickness of 8 mm. All post-processing was run on a 2560 cores Quadro P5000 GPU and 16GB of GDDR5 VRAM.

[5] `https://github.com/CEA-COSMIC/pysap-mri`

4 | RESULTS

4.1 | Coil combination and phase unwrapping

Different algorithms were considered in the estimation pipeline for the coil combination and unwrapping tasks, and results are shown in Fig. 2 and Fig. 3 respectively. The two coil combination algorithms compared in Fig. 2, namely VCC (B) and ACC (C), obtain similar performances for AF=10 (row 1), while an overall degradation can be observed at AF=20 (row 2). The front region close to the sinuses in (B2) with VCC is dominated by noise, making difficult to estimate even visually the unwrapped phase values. On the other hand, the ACC method produces locally consistent results (C2) with only some blurring in the regions associated with the highest off-resonance frequencies, thus obtaining more reliable phase maps.

The phase maps from Fig. 2 are then unwrapped using different algorithms and processed to yield the estimates shown in Fig. 3, respectively using VCC (rows 1,3) and ACC (rows 2,4) methods on both volunteers #1 (rows 1,2) and #3 (rows 3,4). Most unwrapping algorithms are consistent with the reference at AF=10 (rows 1,2) except for Schofield et al.'s [52] method (E). However at AF=20 (rows 3,4), no unwrapping algorithm managed to obtain results close to the reference maps in one step. Particularly, frequency values seem to drop significantly in key regions pointed on (C3) and (D3-4), using respectively Herráez et al.'s [51] and Dymerska et al.'s [53] methods. Such behavior can be detrimental to the additional iteration steps. For the other algorithms the field map remains locally smooth, however its values are underestimated as illustrated in Fig. 3 (B4) and (C4). An improved estimation is achieved in the inner region in (C4) with the method proposed by Herráez et al. [51], balanced by extreme frequencies outside the skull on the left side, also observed in (C1) and (D1). Overall, the approach proposed by Ghiglia et al [50], shown in Fig. 3 (B), is preferred due to the absence of detrimental patterns, particularly when combined with the ACC method [47, 48] shown in rows (2,4).

4.2 | ΔB_0 field map estimation

The first estimation step described previously took approximately 40s to compute on average, with the following details: adjoint NUFFT computation in 16s, coil combination in 5s, phase unwrapping in 8s, and masking, filtering and scaling in 11s. Additional steps may last between 3 and 5 min depending on the number of interpolators L used for correction, which tends to increase at each step. Note that the ΔB_0 correcting pseudo-NUFFT operator [32] can be parallelized with more resources to achieve a duration for additional steps close to 40s as well. Overall, the estimation time contributes marginally to the 6 to 8 hours required to perform the state-of-the-art correction [32].

The intermediate estimation steps are represented in Fig. 4. For both volumes the low-frequency phase is progressively canceled over the iterations while the ΔB_0 map converges. The resulting ΔB_0 maps are shown for all volumes in Fig. 5 along with the acquired reference maps. The phase images obtained after one correction step with the acquired maps are shown on row (4). For each volume, an important phase component remains, particularly in the bucco-nasal regions. This observed phase is wrapped from negative to positive values, almost reaching an entire 2π cycle that corresponds to an inappropriate over-correction of 50 Hz (Eq. (5)). A remaining phase component from other sources is indeed expected in Eq. (4) but those regions are specifically associated with B_0 inhomogeneities and the values are too large to correspond to ΔB_1 or B_e contributions. On the other hand, the estimated maps produce spatially homogeneous phase images (see row (6) in Fig. 5). More details are available in the supplementary materials (Section S7).

A comparison between the estimated and acquired ΔB_0 maps is proposed for all volumes in Fig. 6. As shown in the superimposed histograms, the estimated frequencies tend to be lower than the acquired ones, thus confirming that references might be over-estimated as observed in Fig. 5. Additionally, this is quantitatively assessed through the linear regression slopes around 0.9. The distributions are however similar as shown by the Pearson correlation coefficients $R \geq 0.93$. The RMSE varies from 6.69 Hz for the first volume to 10.80 Hz for the third volume. A noticeable shift of 7.27 Hz is observed for the third volume (originating from the acquired map) although it has the highest R value.

A global specific absorption rate (SAR) of 3% was measured during examinations. Considering a homogeneous temperature rise, the heating contribution to the phase can be roughly estimated around 5 mHz using Eq. (9) (with ν=127.74 MHz, α=-0.01 ppm/°C). This confirms that the temperature contribution to the phase variation can be neglected for the proposed sequence.

4.3 | ΔB_0 artifacts correction

The volumes with SWI processing are displayed in Fig. 7 for AF=10 and Fig. 8 for AF=20 with emphasis on the bucco-nasal region. Overall, the less affected volume by the correction is #2 while the more impacted is #1. This striking difference cannot be explained by acquisition parameters which were similar for both. Besides the main artifact, the shape of the anterior region for volume #1 has indeed become sharper. Stronger artifacts are observed in volumes #3 and #4 along with a larger correction. Quantitative comparisons are available in the supplementary materials (Section S7). Overall, the corrections are improving the image quality for all volumes although some regions cannot be recovered.

While the corrections obtained with the reference and proposed ΔB_0 maps are similar, some noticeable differences persist. On volume #1 (Fig. 7, A), the right part of the brain visible on the axial and coronal views (A2) suffers from degradation only present in the reference correction using the external map. The anterior region previously mentioned recovers a wider area shown with dotted lines when using the estimated map. Almost no difference is visible between the two corrections on volumes #2 and #4 except when comparing the axial slices (Fig. 7, B-C). Finally, both volumes #1 and #3 demonstrate a definite advantage of using the proposed ΔB_0 field map estimation technique compared to using the external ΔB_0 field map.

5 | DISCUSSION

An iterative pipeline was established by comparing two coil combination and four phase unwrapping algorithms in order to produce a robust ΔB_0 field map estimate. The coil combination method from Walsh et al. [47], further improved by Inati et al. [48], along with the phase unwrapping method developed by Ghiglia et al. [50] and embedded in an iterative pipeline permit to obtain a stable ΔB_0 estimation that empirically converged in few iterations. The resulting maps were observed to be highly correlated with the acquired maps used as reference. Improved corrections were generally observed with the proposed method over the references while none of the expected sources of error seemed to impact the correction.

5.1 | ΔB_0 field map estimation

The differences observed between the acquired and estimated ΔB_0 maps have a few distinct causes. The first one to consider is the quality of the acquired ΔB_0 map. The number of echo times and their proximity in time can influence the measurements [14] and thus the computation of the ΔB_0 map using Eq. (6). While two close echoes facilitate the phase unwrapping task, as mentioned in the Theory (Section 2), a third and more distant echo can be used to strengthen the linear regression for peak values, which might otherwise be less accurate [14, 24]. The residual phase shown in Fig. 5 (D) suggests an over-correction and hence that the acquired ΔB_0 field maps are all over-evaluated. Therefore, the difference observed between acquired and estimated ΔB_0 field maps should be considered carefully. Additionally, a mismatch between the external and estimated field maps could also be caused by inter-scan motion, but would not explain the overall lower values in the proposed estimation. The resolution was also suspected to impact the correction [77], but experiments proposed in the supplementary materials (Section S6) showed almost no difference when downsampling the ΔB_0 map estimates. Overall, the external ΔB_0 field maps could be improved in order to provide a better quality assessment of the ΔB_0 map estimation algorithm.

The second element to take into account is the modeling error ϵ involved in Eq. (8). Besides the contributions from the ΔB_1 and B_e fields, the hypothesis of zero-order B_0 shimming was not systematically respected as observed in Fig. 6 through the different constant shifts in the linear regressions. For three volumes, a variation of less than 2 Hz is observed while almost 8 Hz are reached with volume #3. However this difference does not seem to imbalance the correction, as this volume still presents clear improvements using the proposed estimation over the reference.

Finally, the last possible explanation for the observed difference are the methods used in the estimation pipeline. The strongly accelerated acquisitions (AF=20) showed phase degradation near the bucco-nasal region, but still converged to a similar quality of ΔB_0 map estimates as those obtained at AF=10. However, as pointed out in [60], the selected method by Ghiglia et al. [50] is a non-exact method which removes some spatial components of the phase. It could cause the lower estimated frequencies observed in Fig. 6, but would not explain that phase residuals are present in the references rather than in the proposed correction in Fig. 5. An iterative solution allowed us to favor the robustness of the unwrapping algorithm over its accuracy, but more recent methods could be explored to obtain a better compromise in fewer iterations [60, 78].

5.2 | ΔB_0 artifacts correction

In terms of image quality, two volumes (#1, #3) under study showed a clear advantage in using the proposed method. In contrast, for the other two (#2, #4) almost no difference was observed with the references (Fig. 7 and Fig. 8). Volume #4 represents the worst estimation case, as it also has the lowest correlation coefficient between the acquired and estimated ΔB_0 maps (Fig. 6). On volume #1, the degradation brought by the reference correction on the right side of the brain (Fig. 7, A2) could be explained by unexpected inter-scan movements causing a mismatch between the map and the SWI volume. The proposed method overcomes such issue as the ΔB_0 map

is internally extracted from the same data set. Besides the partial correction with both the acquired and estimated ΔB_0 maps, no spatial degradation that could be attributed to the pipeline or the ΔB_1 and B_e fields has been observed. The above mentioned sources of error seem less impactful than the gain issuing from high resolution, robustness to motion and reduced acquisition time.

6 | CONCLUSIONS

MR imaging contrasts based on long readouts tend to suffer from B_0 inhomogeneities and thus from signal dropout, especially in non-Cartesian acquisitions used to reach shorter scan times. On the other hand, long echo times such as in SWI facilitate the estimation of a ΔB_0 field map that can be further used for artifact correction as proposed in this paper. The proposed approach actually relies on the internal phase measurements during SWI acquisition and on some tenable assumptions in regard to its main contributions to produce a high resolution and robust-to-motion ΔB_0 field map in a few minutes only. This approach can be used a posteriori during the image reconstruction step and can deliver equivalent to improved corrections compared to the reference, which requires itself additional scan time. The estimation duration could be reduced in the future by improving the different pipeline steps with more advanced coil combination or phase unwrapping algorithms. Lastly, future work could focus on integrating optimization-based estimation methods to account for bulk motion, or on extending this work from static imaging to EPI, similarly to recent works by Dymerska et al. [19].

Acknowledgments

The concepts and information presented in this article are based on research results that are not commercially available. Future availability cannot be guaranteed. We thank Chaithya G R for his numerous technical contributions, and Dr. Caroline Le Ster and Dr. Alexis Amadon for useful discussions.

References

1 Haacke EM, Xu Y, Cheng YCN, Reichenbach JR. Susceptibility weighted imaging (SWI). Magnetic Resonance in Medicine 2004;52(3):612–618.

2 Wu Z, Mittal S, Kish K, Yu Y, Hu J, Haacke EM. Identification of calcification with MRI using susceptibility-weighted imaging: a case study. Journal of Magnetic Resonance Imaging 2009;29(1):177–182.

3 Pruessmann KP, Weiger M, Börnert P, Boesiger P. Advances in sensitivity encoding with arbitrary k-space trajectories. Magnetic Resonance in Medicine 2001;46(4):638–651.

4 Griswold MA, et al. Generalized autocalibrating partially parallel acquisitions (GRAPPA). Magnetic Resonance in Medicine 2002;47(6):1202–1210.

5 Lustig M, et al. Sparse MRI: The application of compressed sensing for rapid MR imaging. Magnetic Resonance in Medicine 2007;58(6):1182–1195.

6 Seiberlich N, Breuer FA, Blaimer M, Barkauskas K, Jakob PM, Griswold MA. Non-Cartesian data reconstruction using GRAPPA operator gridding (GROG). Magnetic Resonance in Medicine 2007;58(6):1257–1265.

7 Vasanawala SS, Alley MT, Hargreaves BA, Barth RA, Pauly JM, Lustig M. Improved pediatric MR imaging with compressed sensing. Radiology 2010;256(2):607–616.

8 Boyer C, et al. On the generation of sampling schemes for MRI. SIAM Imaging Sciences 2016;9(4):2039–2072.

9 Luo T, Noll DC, Fessler JA, Nielsen JF. A GRAPPA algorithm for arbitrary 2D/3D non-Cartesian sampling trajectories with rapid calibration. Magnetic resonance in Medicine 2019;82(3):1101–1112.

10 Polak D, Cauley S, Huang SY, Longo MG, Conklin J, Bilgic B, et al. Highly-accelerated volumetric brain examination using optimized wave-CAIPI encoding. Journal of Magnetic Resonance Imaging 2019;50(3):961–974.

11 Lazarus C, Weiss P, Chauffert N, Mauconduit F, El Gueddari L, Destrieux C, et al. SPARKLING: variable-density k-space filling curves for accelerated T2*-weighted MRI. Magnetic Resonance in Medicine 2019;81(6):3643–3661.

12 Lazarus C, Weiss P, El Gueddari L, Mauconduit F, Massire A, Ripart M, et al. 3D variable-density SPARKLING trajectories for high-resolution T2*-weighted magnetic resonance imaging. NMR in Biomedicine 2020;33(9):e4349.

13 Chaithya G, Weiss P, Massire A, Vignaud A, Ciuciu P. Optimizing full 3D SPARKLING trajectories for high-resolution T2*-weighted magnetic resonance imaging; 2021.

14 de Graaf RA, Juchem C. B0 Shimming Technology. In: Magnetic Resonance Technology; 2016.p. 166–207.

15 Yudilevich E, Stark H. Spiral sampling in magnetic resonance imaging-the effect of inhomogeneities. IEEE transactions on medical imaging 1987;6(4):337–345.

16 Gruetter R. Automatic, localized in vivo adjustment of all first-and second-order shim coils. Magnetic Resonance in Medicine 1993;29(6):804–811.

17 Wachowicz K. Evaluation of active and passive shimming in magnetic resonance imaging. Research and Reports in Nuclear Medicine 2014;4:1–12.

18 Sati P, Thomasson D, Li N, Pham D, Biassou N, Reich D, et al. Rapid, high-resolution, whole-brain, susceptibility-based MRI of multiple sclerosis. Multiple Sclerosis Journal 2014;20(11):1464–1470.

19 Dymerska B, Poser BA, Barth M, Trattnig S, Robinson SD. A method for the dynamic correction of B0-related distortions in single-echo EPI at 7 T. Neuroimage 2018;168:321–331.

20 Weiger M, Pruessmann KP, Österbauer R, Börnert P, Boesiger P, Jezzard P. Sensitivity-encoded single-shot spiral imaging for reduced susceptibility artifacts in BOLD fMRI. Magnetic Resonance in Medicine: An Official Journal of the International Society for Magnetic Resonance in Medicine 2002;48(5):860–866.

21 Wilm BJ, Barmet C, Gross S, Kasper L, Vannesjo SJ, Haeberlin M, et al. Single-shot spiral imaging enabled by an expanded encoding model: Demonstration in diffusion MRI. Magnetic resonance in medicine 2017;77(1):83–91.

22 Kasper L, Engel M, Barmet C, Haeberlin M, Wilm BJ, Dietrich BE, et al. Rapid anatomical brain imaging using spiral acquisition and an expanded signal model. NeuroImage 2018;168:88–100.

23 Aghaeifar A, Zhou J, Heule R, Tabibian B, Schölkopf B, Jia F, et al. A 32-channel multi-coil setup optimized for human brain shimming at 9.4 T. Magnetic Resonance in Medicine 2020;83(2):749–764.

24 Pinho-Meneses B, Amadon A. A fieldmap-driven few-channel shim coil design for MRI of the human brain. Physics in Medicine & Biology 2021;66(1):015001.

25 Pinho-Meneses B, Amadon A. Physical Limits to Human Brain B0 Shimming, Engineering Implications Thereof; 2021, `https://hal.archives-ouvertes.fr/hal-03210241`, working paper or preprint.

26 Andersson JL, Skare S, Ashburner J. How to correct susceptibility distortions in spin-echo echo-planar images: application to diffusion tensor imaging. Neuroimage 2003;20(2):870–888.

27 Fritz L, Mulders J, Breman H, Peters J, Bastiani M, Roebroeck A, et al. Comparison of EPI distortion correction methods at 3T and 7T. In: Poster Presented at the Annual Meeting of the Organization for Human Brain Mapping Hamburg, Germany; 2014. .

28 Noll DC. Multishot rosette trajectories for spectrally selective MR imaging. IEEE transactions on medical imaging 1997;16(4):372–377.

29 Noll DC, Meyer CH, Pauly JM, Nishimura DG, Macovski A. A homogeneity correction method for magnetic resonance imaging with time-varying gradients. IEEE transactions on medical imaging 1991;10(4):629–637.

30 Man LC, Pauly JM, Macovski A. Multifrequency interpolation for fast off-resonance correction. Magnetic Resonance in Medicine 1997;37(5):785–792.

31 Sutton BP, Noll DC, Fessler JA. Fast, iterative image reconstruction for MRI in the presence of field inhomogeneities. IEEE transactions on medical imaging 2003;22(2):178–188.

32 Fessler JA, Lee S, Olafsson VT, Shi HR, Noll DC. Toeplitz-based iterative image reconstruction for MRI with correction for magnetic field inhomogeneity. IEEE Transactions on Signal Processing 2005;53(9):3393–3402.

33 Ostenson J, Robison RK, Zwart NR, Welch EB. Multifrequency interpolation in spiral magnetic resonance fingerprinting for correction of off-resonance blurring. Magnetic resonance imaging 2017;41:63–72.

34 Man LC, Pauly JM, Macovski A. Improved automatic off-resonance correction without a field map in spiral imaging. Magnetic Resonance in Medicine 1997;37(6):906–913.

35 Sutton BP, Noll DC, Fessler JA. Dynamic field map estimation using a spiral-in/spiral-out acquisition. Magnetic Resonance in Medicine: An Official Journal of the International Society for Magnetic Resonance in Medicine 2004;51(6):1194–1204.

36 Patzig F, Wilm B, Gross S, Brunner D, Pruessmann KP. Off-Resonance Self-Correction for Single-Shot Imaging. In: Proceedings of the 28th Annual Meeting of ISMRM Virtual; 2020. p. 3400.

37 Patzig F, Wilm B, Pruessmann KP. Off-Resonance Self-Correction by Implicit B0-Encoding. In: Proceedings of the 29th Annual Meeting of ISMRM Virtual; 2021. p. 666.

38 Salomir R, de Senneville BD, Moonen CT. A fast calculation method for magnetic field inhomogeneity due to an arbitrary distribution of bulk susceptibility. Concepts in Magnetic Resonance Part B: Magnetic Resonance Engineering: An Educational Journal 2003;19(1):26–34.

39 Lee SK, Hwang SH, Barg JS, Yeo SJ. Rapid, theoretically artifact-free calculation of static magnetic field induced by voxelated susceptibility distribution in an arbitrary volume of interest. Magnetic Resonance in Medicine 2018;80(5):2109–2121.

40 Eckstein K, Bachrata B, Hangel G, Widhalm G, Enzinger C, Barth M, et al. Improved susceptibility weighted imaging at ultra-high field using bipolar multi-echo acquisition and optimized image processing: CLEAR-SWI. NeuroImage 2021;237:118175.

41 Baron CA, Nishimura DG. B0 mapping using rewinding trajectories (BMART). Magnetic Resonance in Medicine 2017;78(2):664–669.

42 Robinson S, Grabner G, Witoszynskyj S, Trattnig S. Combining phase images from multi-channel RF coils using 3D phase offset maps derived from a dual-echo scan. Magnetic resonance in medicine 2011;65(6):1638–1648.

43 Kimmlingen R. Magnetic field gradients. In: Magnetic Resonance Technology; 2016.p. 208–263.

44 De Graaf RA. In vivo NMR spectroscopy: principles and techniques. John Wiley & Sons; 2019.

45 Roemer PB, Edelstein WA, Hayes CE, Souza SP, Mueller OM. The NMR phased array. Magnetic Resonance in Medicine 1990;16(2):192–225.

46 Parker DL, Payne A, Todd N, Hadley JR. Phase reconstruction from multiple coil data using a virtual reference coil. Magnetic Resonance in Medicine 2014;72(2):563–569.

47 Walsh DO, Gmitro AF, Marcellin MW. Adaptive reconstruction of phased array MR imagery. Magnetic Resonance in Medicine: An Official Journal of the International Society for Magnetic Resonance in Medicine 2000;43(5):682–690.

48 Inati SJ, Hansen MS, Kellman P. A Solution to the Phase Problem in Adaptive Coil Combination. In: Proceedings of the 21st Annual Meeting of ISMRM Salt Lake City, Utah, USA; 2013. p. 2672.

49 Inati SJ, Hansen MS, Kellman P. A Fast Optimal Method for Coil Sensitivity Estimation and Adaptive Coil Combination for Complex Images. In: Proceedings of the 22nd Annual Meeting of ISMRM Milan, Italy; 2014. p. 4407.

50 Ghiglia DC, Romero LA. Robust two-dimensional weighted and unweighted phase unwrapping that uses fast transforms and iterative methods. JOSA A 1994;11(1):107–117.

51 Herráez MA, Burton DR, Lalor MJ, Gdeisat MA. Fast two-dimensional phase-unwrapping algorithm based on sorting by reliability following a noncontinuous path. Applied optics 2002;41(35):7437–7444.

52 Schofield MA, Zhu Y. Fast phase unwrapping algorithm for interferometric applications. Optics letters 2003;28(14):1194–1196.

53 Dymerska B, Eckstein K, Bachrata B, Siow B, Trattnig S, Shmueli K, et al. Phase unwrapping with a rapid opensource minimum spanning tree algorithm (ROMEO). Magnetic Resonance in Medicine 2021;85(4):2294–2308.

54 Doneva M. Mathematical models for magnetic resonance imaging reconstruction: An overview of the approaches, problems, and future research areas. IEEE Signal Processing Magazine 2020;37(1):24–32.

55 Hunt BR. Matrix formulation of the reconstruction of phase values from phase differences. J Opt Soc Am 1979 Mar;69(3):393–399.

56 Chung S, Kim D, Breton E, Axel L. Rapid B1+ mapping using a preconditioning RF pulse with TurboFLASH readout. Magnetic resonance in medicine 2010;64(2):439–446.

57 Van Lier ALHMW, Brunner DO, Pruessmann KP, Klomp DW, Luijten PR, Lagendijk JJ, et al. B1 Phase mapping at 7 T and its application for in vivo electrical conductivity mapping. Magnetic Resonance in Medicine 2012;67(2):552–561.

58 Le Ster C, Mauconduit F, Mirkes C, Bottlaender M, Boumezbeur F, Djemai B, et al. RF heating measurement using MR thermometry and field monitoring: Methodological considerations and first in vivo results. Magnetic Resonance in Medicine 2021;85(3):1282–1293.

59 Van de Moortele PF, Pfeuffer J, Glover GH, Ugurbil K, Hu X. Respiration-induced B0 fluctuations and their spatial distribution in the human brain at 7 Tesla. Magnetic Resonance in Medicine: An Official Journal of the International Society for Magnetic Resonance in Medicine 2002;47(5):888–895.

60 Robinson SD, Bredies K, Khabipova D, Dymerska B, Marques JP, Schweser F. An illustrated comparison of processing methods for MR phase imaging and QSM: combining array coil signals and phase unwrapping. NMR in Biomedicine 2017;30(4):e3601.

61 Vaidya M, Collins C, Sodickson D, Brown R, Wiggins G, Lattanzi R. Dependence of B1- and B1+ field patterns of surface coils on the electrical properties of the sample and the MR operating frequency. Concepts in Magnetic Resonance Part B: Magnetic Resonance Engineering 2016;46(1):25–40.

62 Brodsky EK, Klaers JL, Samsonov AA, Kijowski R, Block WF. Rapid measurement and correction of phase errors from B0 eddy currents: Impact on image quality for non-Cartesian imaging. Magnetic resonance in medicine 2013;69(2):509–515.

63 Hedley M, Yan H. Motion artifact suppression: a review of post-processing techniques. Magnetic resonance imaging 1992;10(4):627–635.

64 Welch EB, Manduca A, Grimm RC, Ward HA, Jack Jr CR. Spherical navigator echoes for full 3D rigid body motion measurement in MRI. Magnetic Resonance in Medicine: An Official Journal of the International Society for Magnetic Resonance in Medicine 2002;47(1):32–41.

65 Van Rossum G, Drake Jr FL. Python tutorial, vol. 620. Centrum voor Wiskunde en Informatica Amsterdam; 1995.

66 Okuta R, Unno Y, Nishino D, Hido S, Loomis C. CuPy: A NumPy-Compatible Library for NVIDIA GPU Calculations. In: Proceedings of Workshop on Machine Learning Systems (LearningSys) in The Thirty-first Annual Conference on Neural Information Processing Systems (NIPS), vol. 6 Long Beach, CA, USA; 2017. .

67 Baldi A, Bertolino F, Ginesu F. Phase unwrapping algorithms: a comparison. In: Interferometry in Speckle Light Springer; 2000.p. 483–490.

68 Van der Walt S, Schönberger JL, Nunez-Iglesias J, Boulogne F, Warner JD, Yager N, et al. scikit-image: image processing in Python. PeerJ 2014;2:e453.

69 Bezanson J, Edelman A, Karpinski S, Shah VB. Julia: A fresh approach to numerical computing. SIAM review 2017;59(1):65–98.

70 Metere R, Möller HE. PyMRT and DCMPI: Two new Python packages for MRI data analysis. In: Proceedings of the 25th Annual Meeting of ISMRM Honolulu, HI, USA; 2017. p. 3816.

71 Buehrer M, Pruessmann KP, Boesiger P, Kozerke S. Array compression for MRI with large coil arrays. Magnetic Resonance in Medicine 2007;57(6):1131–1139.

72 Knoll F, Schwarzl A, Diwoky C, Sodickson DK. gpuNUFFT-an open source GPU library for 3D regridding with direct Matlab interface. In: Proceedings of the 22nd Annual Meeting of ISMRM Milan, Italy; 2014. p. 4297.

73 Pipe JG, Menon P. Sampling density compensation in MRI: rationale and an iterative numerical solution. Magnetic Resonance in Medicine: An Official Journal of the International Society for Magnetic Resonance in Medicine 1999;41(1):179–186.

74 Farrens S, Grigis A, El Gueddari L, Ramzi Z, Chaithya G, Starck S, et al. PySAP: Python Sparse Data Analysis Package for multidisciplinary image processing. Astronomy and Computing 2020;32:100402.

75 El Gueddari L, Chaithya G, Ramzi Z, Farrens S, Starck S, Grigis A, et al. PySAP-MRI: a Python Package for MR Image Reconstruction. In: ISMRM workshop on Data Sampling and Image Reconstruction Sedona, AZ, United States; 2020. https://hal.inria.fr/hal-02399267.

76 El Gueddari L, Lazarus C, Carrié H, Vignaud A, Ciuciu P. Self-calibrating nonlinear reconstruction algorithms for variable density sampling and parallel reception MRI. In: 2018 IEEE 10th Sensor Array and Multichannel Signal Processing Workshop (SAM) Sheffield, UK: IEEE; 2018. p. 415–419.

77 Dubovan P, Kasper L, Uludag K, Baron C. On the impact of B0 map resolution and undersampling on reconstructions using expanded encoding models. In: Proceedings of the 29th Annual Meeting of ISMRM Virtual; 2021. p. 892.

78 Zhao Z, Zhang H, Ma C, Fan C, Zhao H. Comparative study of phase unwrapping algorithms based on solving the Poisson equation. Measurement Science and Technology 2020;31(6):065004.

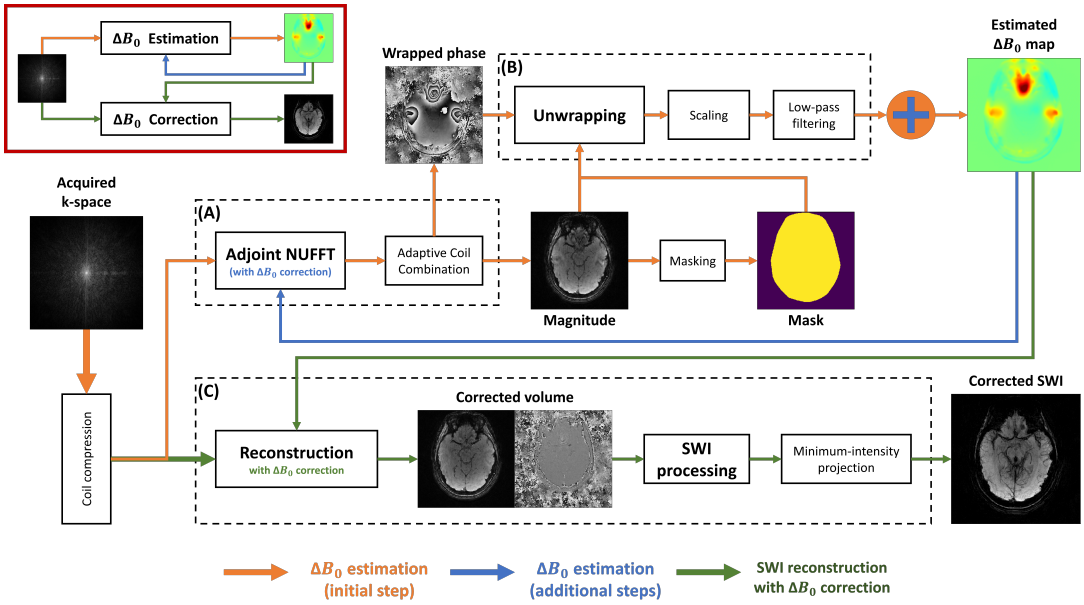

FIGURE 1 Pipeline for ΔB_0 iterative estimation followed by SWI reconstruction.
The pipeline represents the overall process of ΔB_0 estimation (A, B) and the reconstruction with B_0 inhomogeneity correction (C). A simplified version is displayed in the upper left corner for clarification purpose. In block (A), the under-sampled acquired k-space is transformed into a complex-valued volume, then converted in block (B) into the required ΔB_0 field map. Blocks (A)-(B) can be looped over for a few iterations to ensure a robust estimation (blue arrows) by adding residual estimations from each step (orange-circled blue plus sign). The produced field map is then used along with the under-sampled k-space in block (C) to obtain the corrected SWI volume.

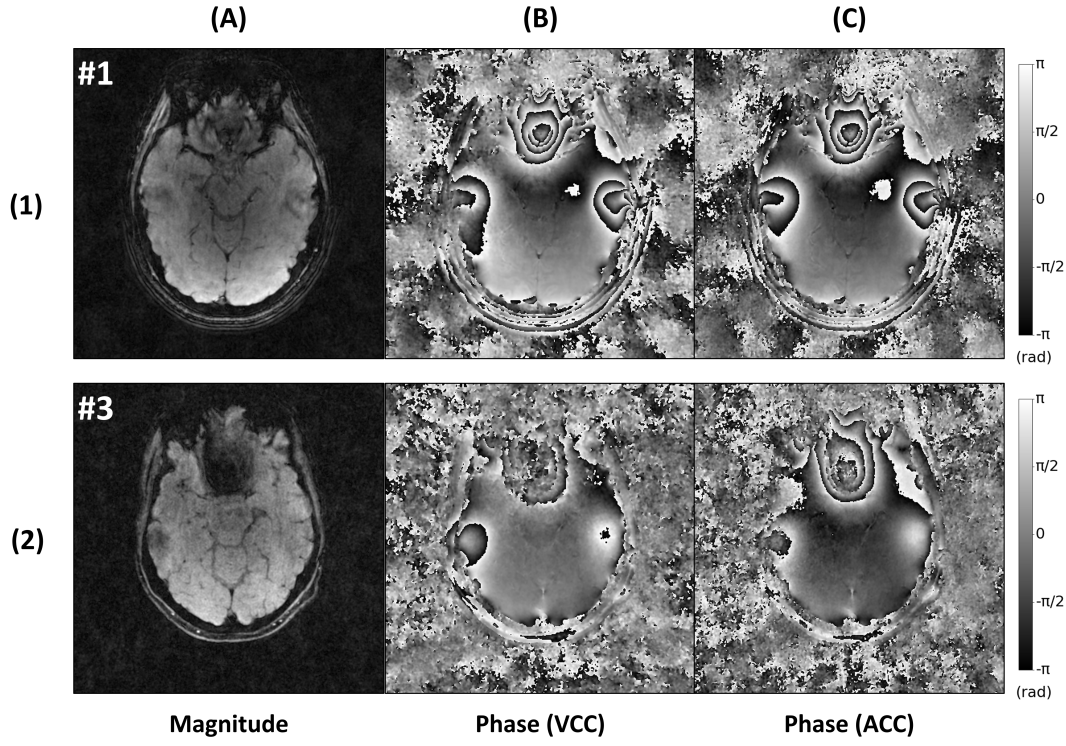

FIGURE 2 Comparison between coil combination algorithms from one-step reconstruction.
Two algorithms are compared one another to combine the 5 channels used during the ΔB_0 map estimation process over volunteer #1 (1) with AF=10 and volunteer #3 (2) with AF=20. The magnitude (A), displayed to help identify the ΔB_0 artifacts, was considered identical in both cases. The phases obtained using the VCC algorithm (B) and the ACC algorithm (C) are shown to compare the degradation of the information caused by B_0 field inhomogeneities in both cases.

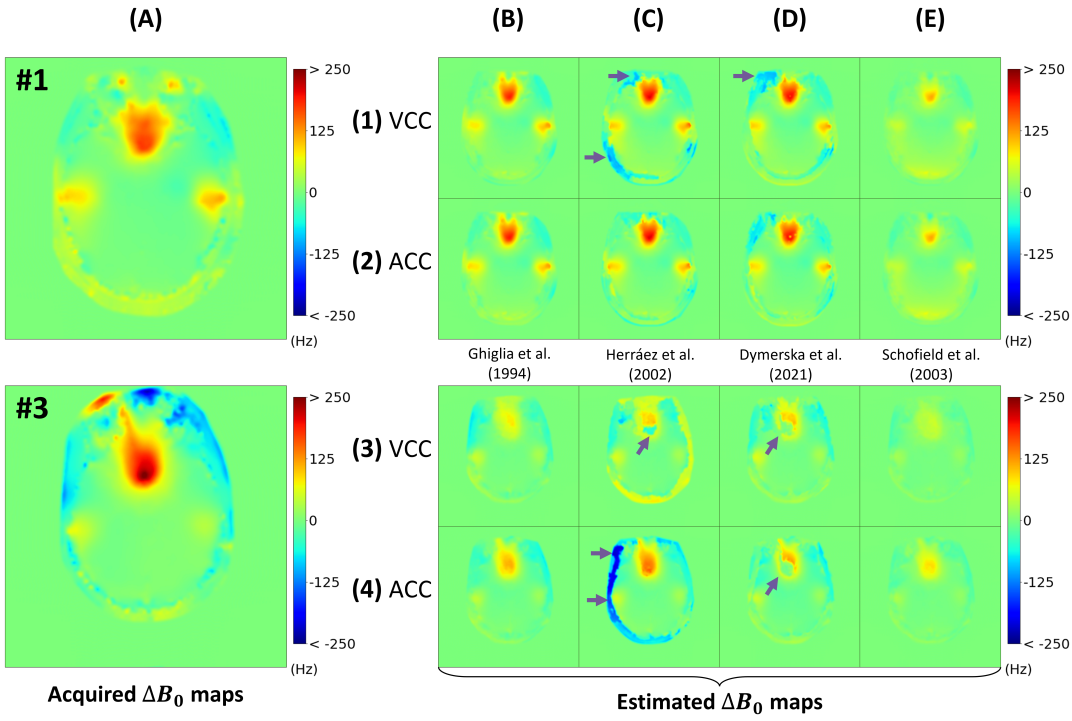

FIGURE 3 **One-step estimations using different coil combination and phase unwrapping methods.** Different algorithms are compared one another to estimate the ΔB_0 maps over two volumes from the phase maps shown in Fig. 2: top rows (1,2) are obtained from volunteer #1 with AF=10, and bottom rows (3, 4) are obtained from volunteer #3 with AF=20. The virtual coil combination (1,3) and the adaptive coil combination (2,4) techniques are used to obtain the wrapped phase maps. Different unwrapping algorithms are then used in all four situations to produce maps (B)-(E) close to those acquired one (A): Ghiglia et al. [50] (B), Herràez et al. [51] (C), Dymerska et al. [53] (D) and Schofield et al. [52] (E). Note that all ΔB_0 field maps were masked post-estimation.

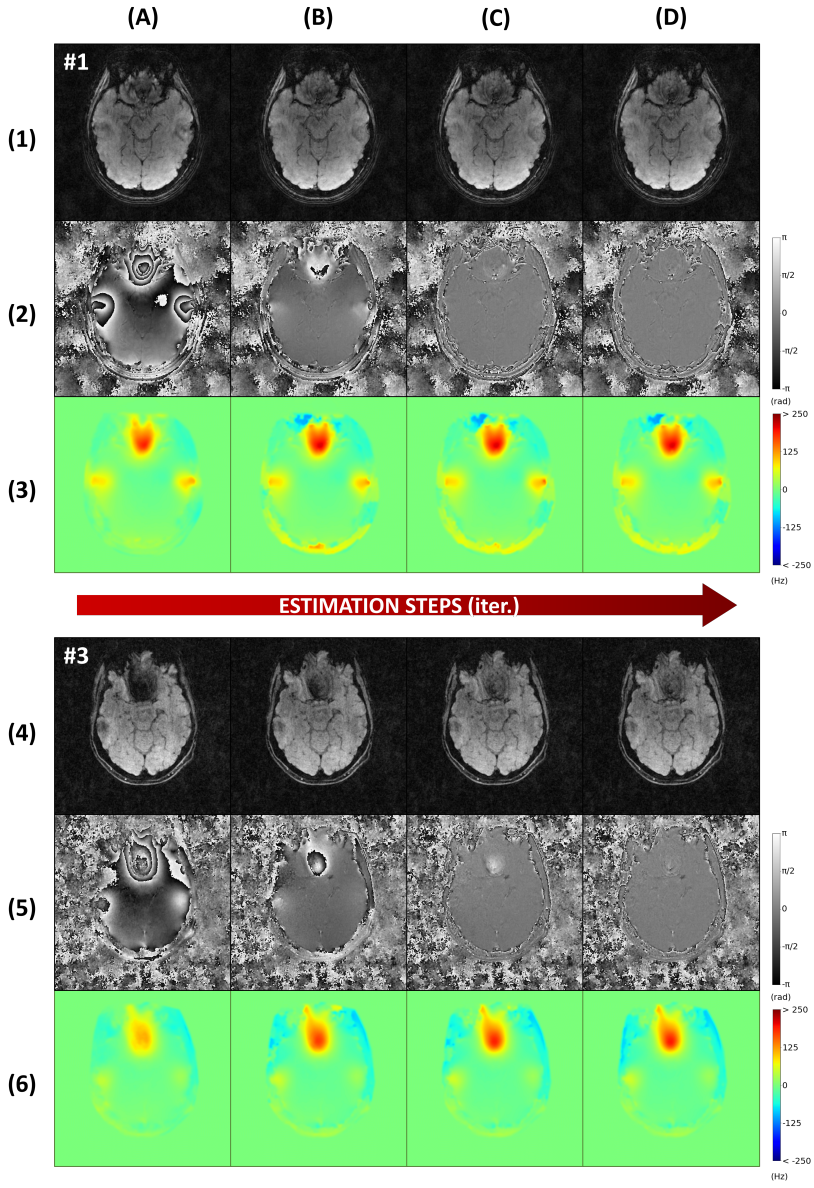

FIGURE 4 **Iterative estimation using the selected pipeline.**
The four-iteration estimation process is illustrated from columns (A) to (D) over two volumes to show the evolution of their ΔB_0 map estimates: top rows (1-3) are obtained from volunteer #1 with AF=10, and bottom rows (4-6) are obtained from volunteer #3 with AF=20. Rows (1) and (4) correspond to the magnitude images, rows (2) and (5) to the wrapped phase images, and rows (3) and (6) to the iterative estimated ΔB_0 field maps obtained from (1,2) and (4,5), respectively.

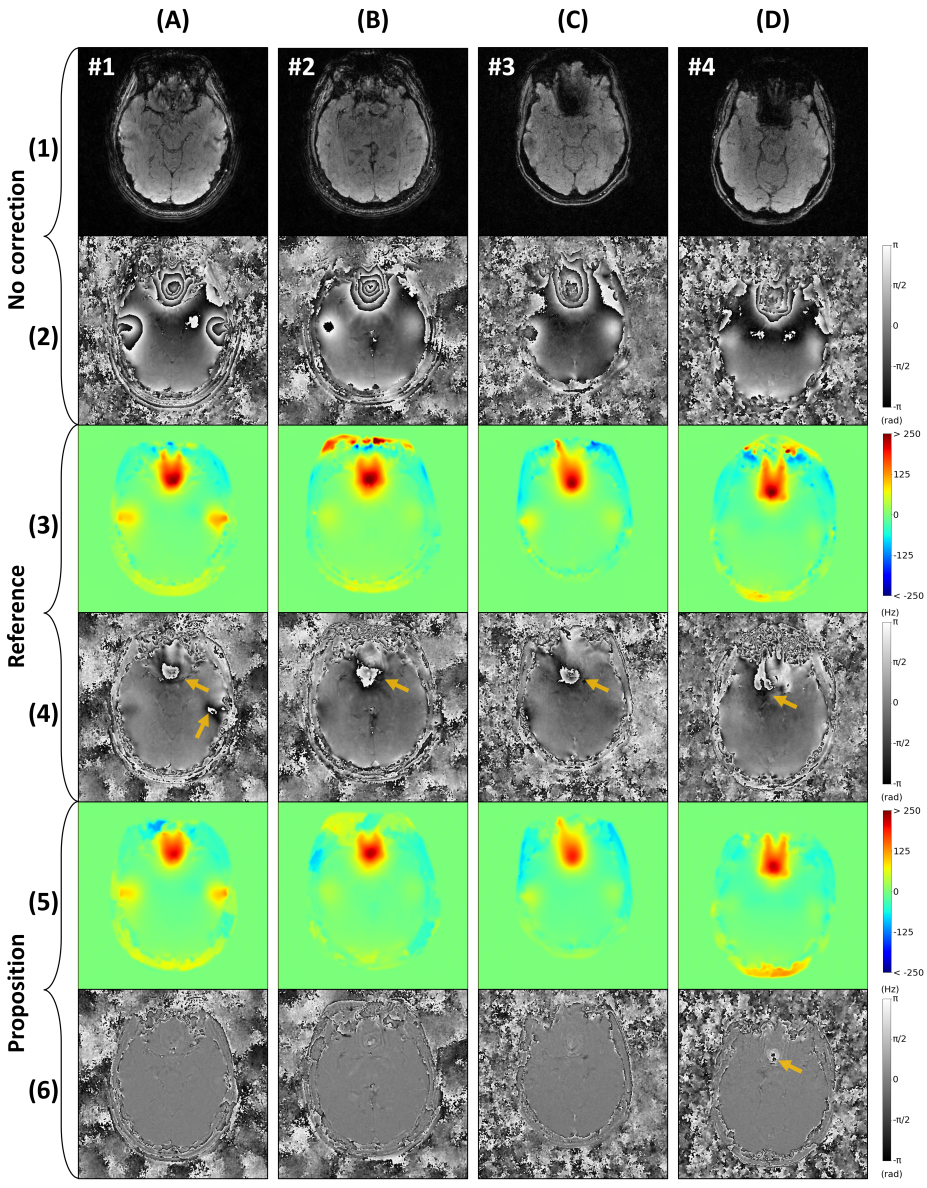

FIGURE 5 **Comparison of the ΔB_0 field maps and the resulting phase images.**
All four volumes are displayed from left to right in columns (A) to (D), respectively. Rows (1) and (2) correspond to the uncorrected magnitude and phase images, (3) to the acquired ΔB_0 field maps used to produce the corrected phase images (4) after one iteration, and (5) to the estimated ΔB_0 field maps used to produce the corrected phase images (6) after one iteration.

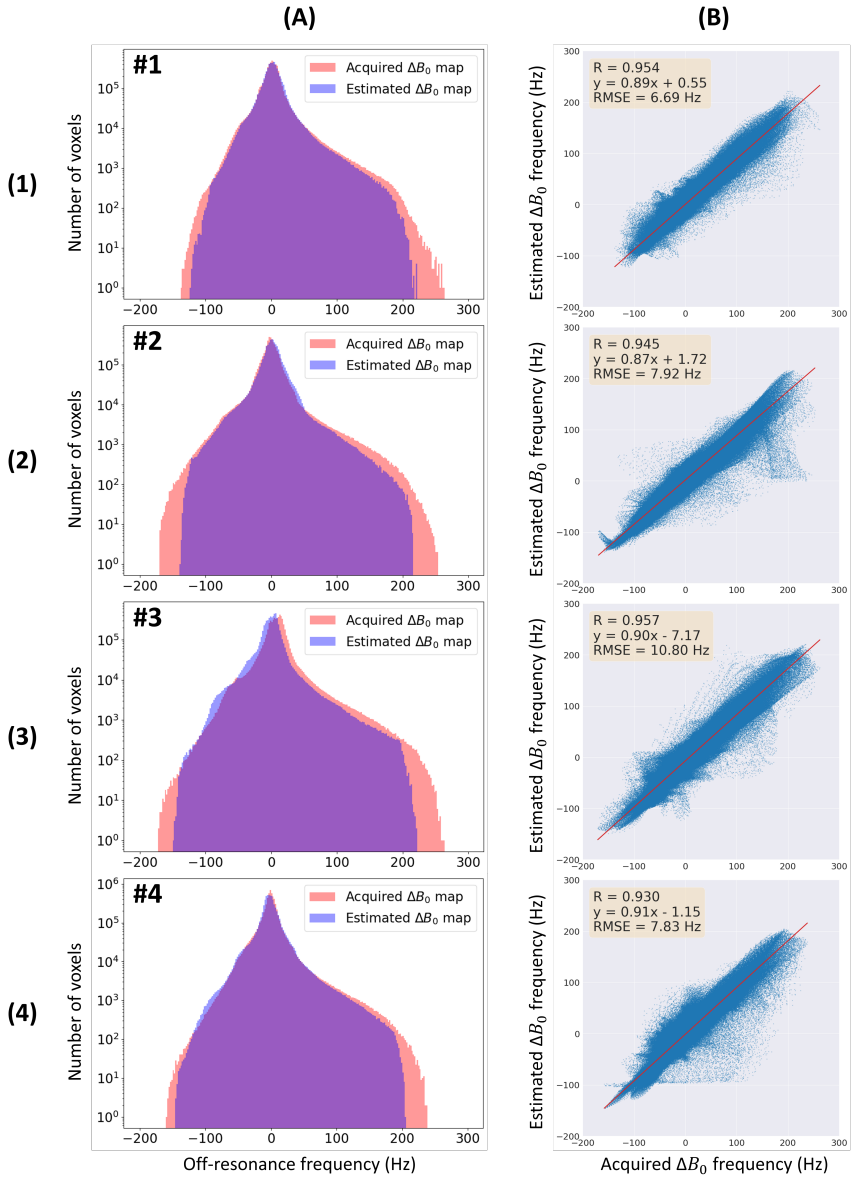

FIGURE 6 Comparison between acquired and estimated ΔB_0 maps.
The acquired and estimated ΔB_0 field maps are confronted one another through superimposed histograms (A) and linear regressions (B) over the spherical stacks of SPARKLING acquisitions (1,2) with AF=10 and the full 3D SPARKLING acquisitions (3,4) with AF=20.

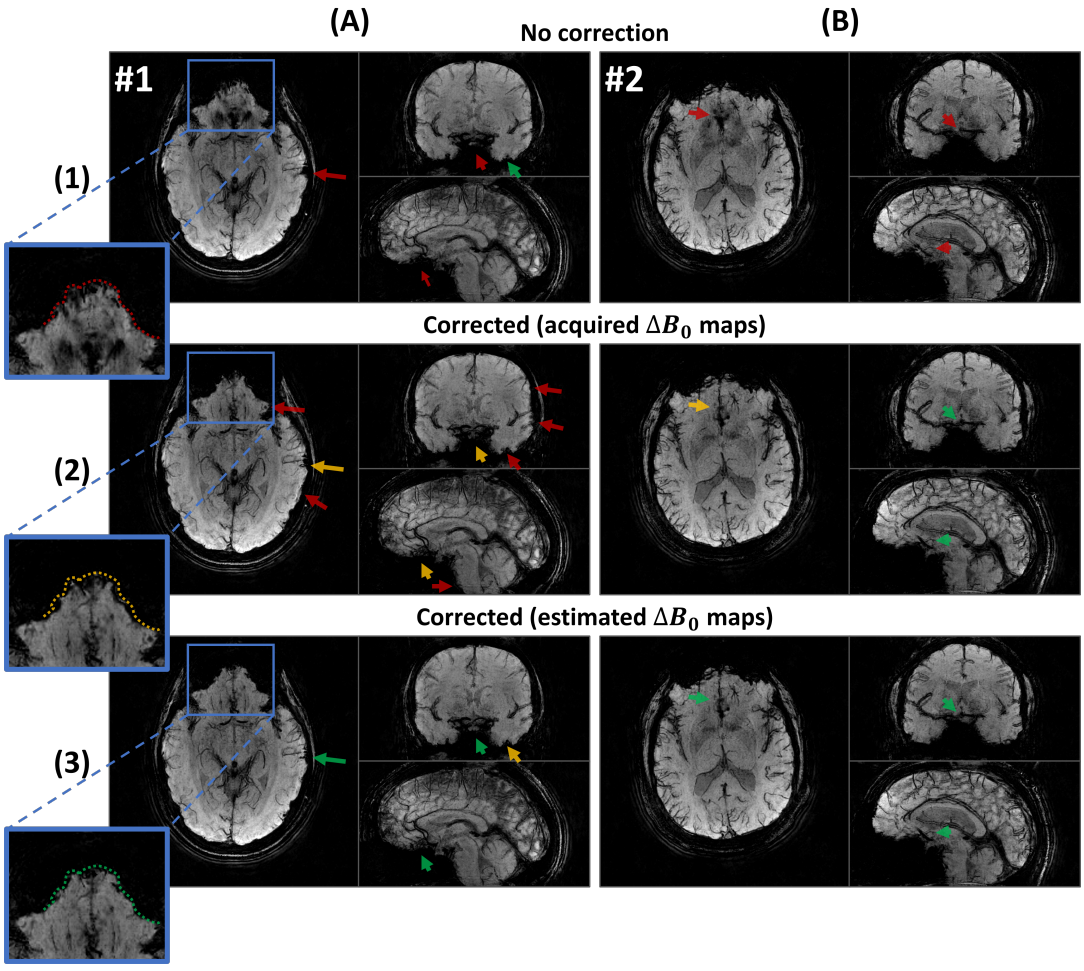

FIGURE 7 **Comparison of ΔB_0 correction with acquired and estimated maps for AF=10.** The different volumes obtained from the spherical stack of SPARKLING acquisitions on volunteers #1 and #2 with AF=10, SWI processing and a 8 mm minimum intensity projection (mIP) are displayed on the left column (A) and right column (B) respectively, according to the following conventions: without ΔB_0 correction in row (1), corrected using acquired ΔB_0 field maps in row (2), corrected using the estimated ΔB_0 field maps in row (3). Different artifact and correction details are pointed out using the following color-coded arrows: artifacted (red), mitigated (orange) and corrected (green). The dotted lines overlaid to the frontal lobe in the axial views of column (1) are used to project the edges from (A1) onto (A2) and (B3) for comparison purpose.

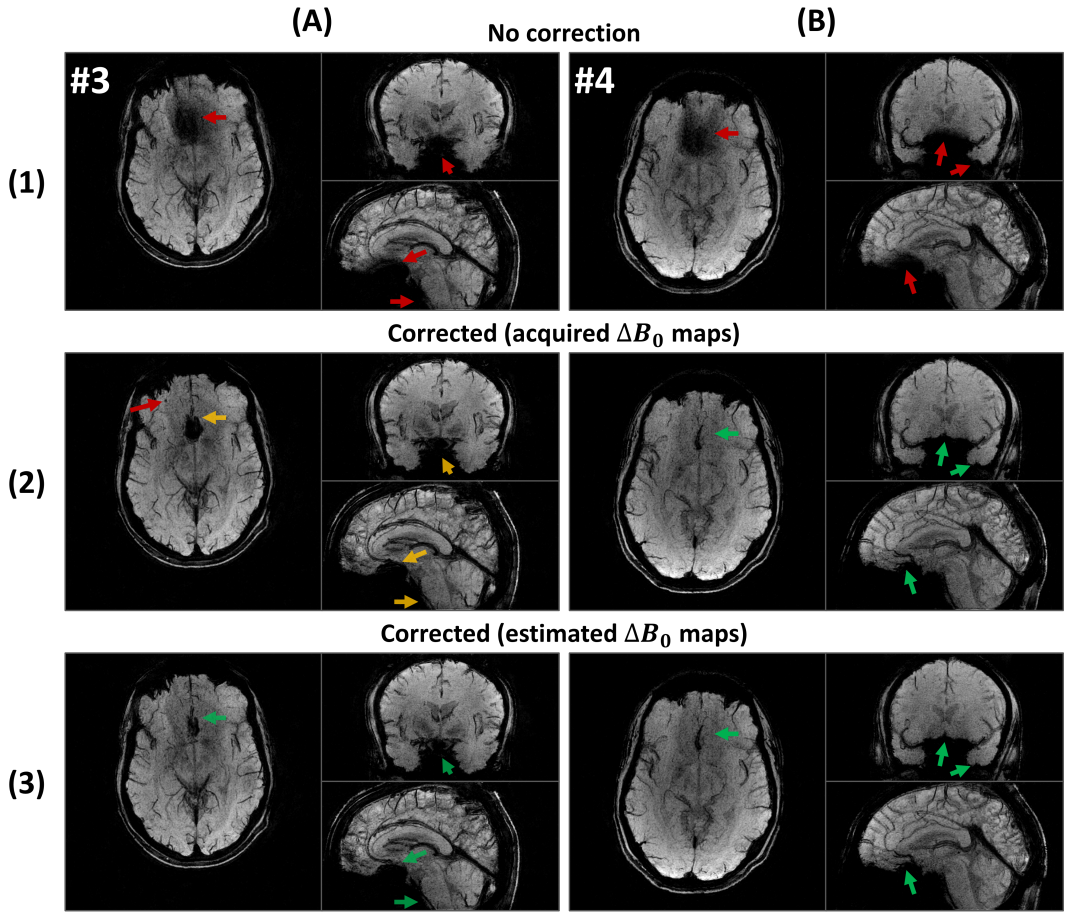

FIGURE 8 **Comparison of ΔB_0 correction with acquired and estimated maps for AF=20.** The different volumes obtained from the full 3D SPARKLING acquisitions on volunteers #3 and #4 with AF=20, SWI processing and a 8 mm minimum intensity projection (mIP) are displayed on the left column (A) and right column (B) respectively, according to the following conventions: without ΔB_0 correction in row (1), corrected using acquired ΔB_0 field maps in row (2), corrected using the estimated ΔB_0 field maps in row (3). Different artifact and correction details are pointed out using the following color-coded arrows: artifacted (red), mitigated (orange) and corrected (green).